IEEE Access
Multidisciplinary | Rapid Review | Open Access Journal

Received October 15, 2020, accepted October 30, 2020, date of publication November 3, 2020, date of current version November 17, 2020.

Digital Object Identifier 10.1109/ACCESS.2020.3035657

Wearable Electromagnetic Belt for Steatotic Liver Detection Using Multivariate Energy Statistics

SASAN AHDI REZAEIEH[1], (Member, IEEE), AIDA BRANKOVIC[1], (Member, IEEE), AZIN S. JANANI[1], BEADAA MOHAMMED[1], (Member, IEEE), AMIN DARVAZEHBAN[1], (Student Member, IEEE), ALI ZAMANI[1], (Member, IEEE), GRAEME A. MACDONALD[2,3], AND AMIN M. ABBOSH[1], (Senior Member, IEEE)

[1]School of Information Technology and Electrical Engineering, The University of Queensland, Brisbane, QLD 4072, Australia
[2]Princess Alexandra-Southside Clinical School, The University of Queensland, Woolloongabba, QLD 4072, Australia
[3]Department of Gastroenterology and Hepatology, Princess Alexandra Hospital, Woolloongabba, QLD 4072, Australia

Corresponding author: Sasan Ahdi Rezaeieh (s.ahdirezaeieh@uq.edu.au)

This work was supported in part by The University of Queensland Philanthropic Grant under Grant 2018002397 and Cooperative Research Centers Projects CRC-P-516.

ABSTRACT A wearable electromagnetic belt system for the detection of hepatic steatosis (lipid accumulation within the major liver cells, hepatocytes), is proposed. To satisfy the requirements of the belt system, an array of body matched antennas is designed. The belt, which goes around the lower chest and over the liver, requires compact, wideband, unidirectional antennas that operate at low microwave frequencies. To avoid using conventional bulky reflector structures, the designed antenna utilizes the loop-dipole combination concept. To enhance electromagnetic wave penetration, the antenna is designed to match the human body. Thus, thanks to the high dielectric loading from the human body, the dipole element of the antenna is easily miniaturized. Since the same principle does not apply on the loop structure, meandered arc-shapes are employed to increase the effective electrical length of the loop. The final antenna design has a measured wide operating bandwidth of 0.58-1.6 GHz with a compact size of $0.096 \times 0.048 \times 0.048\lambda^3$. The proposed structure is effective in irradiating the torso, where the signal can reach center of the liver at a depth of 90 mm, with 64% of the peak radiated power. An electromagnetic belt is built using twelve elements of the designed antennas. The belt is then tested on a 3D printed torso phantom that includes models of the lungs and liver. Due to close dielectric properties of the other tissues inside the torso, these are represented using an average tissue mimicking mixture with permittivity of 46. Measured data are analyzed using multivariate energy statistics method. A peak measured dissimilarity of 15.1% between steatotic and healthy liver is attained. These initial tests and obtained results indicate the potential of the proposed system as a method to diagnose hepatic steatosis.

INDEX TERMS Body-matched antenna, electromagnetic belt, fatty liver disease, statistical based analysis, wearable system.

I. INTRODUCTION

The advancements in signal processing and computational electromagnetics such as tomography techniques have created a great opportunity to expand the development of electromagnetic (EM) diagnostic systems for a wide range of medical conditions [1]–[4]. In the past decade, the main focus has been on breast cancer [4], [5] and head imaging [1], [6] alongside microwave ablation [7] and hyperthermia [8]. These technologies have resulted in improvements in clinical care, and provide impetus to explore new research capacities in this area. Thoracic scanning has been one of these recent developments, with focus on diseases such as heart failure, pleural effusion and lung cancer detection [9], [10]. Researchers studied the possibility of diagnosing pathology inside the chest by monitoring the changes in the phase and amplitude of reflected or transmitted signals [11]. These efforts were later complemented by frequency-based signal processing techniques to generate two- and three-dimensional images [12]. These methods, which are radar-based diagnostic techniques, operate on the concept that any changes in the dielectric properties of tissues would change the distribution

The associate editor coordinating the review of this manuscript and approving it for publication was Davide Comite.

of electric field inside the imaged domain. To that end, the potential of this approach to diagnose hepatic steatosis, based on the EM properties of resected steatotic and non-steatotic liver tissue, appears feasible [13].

Hepatic Steatosis occurs in several clinical situations including in relation to obesity and type 2 diabetes, and with hazardous alcohol consumption. In patients with obesity, the accumulation of fat in the liver is described as non-alcoholic fatty liver disease (NAFLD). This is the most prevalent liver disease in western countries affecting one third of the adult population [14]. In NAFLD, lipid, predominantly triglyceride, accumulates as droplets within liver cells [15]. The accumulation of fat inside the liver creates a contrast between the dielectric properties of a healthy liver ($\epsilon_r = 46$ at 1GHz) [16] and one that is steatotic ($\epsilon_r = 36$ at 1GHz) [17]. Current imaging modalities such as Ultrasound (US), Computerized Tomography (CT), and magnetic resonance imaging (MRI) have poor sensitivity for the diagnosis of hepatic steatosis. Their poor sensitivity and the use of ionizing radiation (CT) or strong magnetic field (MRI), mean that these modalities are not suitable to monitor NAFLD over time. In addition, due to the fixed cavity size for CT and MRI, and weight restrictions for the tables that patient lie on for CT and MRI, obese people above a certain weight and body size cannot be accommodated. The limitations of current systems and potential of EM techniques encourage the design of an adjustable electromagnetic belt for the diagnosis of hepatic steatosis.

The main blocks to the development of an electromagnetic detection system are hardware elements, mainly the antennas, and the software including signal processing and/or image creation algorithms. While the concept of EMI systems is simple, their realization for practical applications is challenging due to the conflicting requirements of hardware and software. EMI systems require to operate at a wideband within lower microwave frequencies of around 0.5-2 GHz [10], yet require compact size to fit around the patient. The selected low microwave frequencies for the design provide a reasonable compromise between the required signal penetration into the lossy torso and resolution needed for detection [18], [19]. The antennas must direct energy in one direction, thus requiring a reflector, yet should be light and portable. To tackle these challenges, several innovative methods have been proposed in the literature. Metamaterial loading [20], [21], dielectric loading [22], dielectric resonators [23], folding and meandering techniques [24] and loop-dipole [25]–[27] combinations have been studied. Despite their notable achievements, these techniques suffer from narrow bandwidth, high profile, heavy structure, low front to back ratio (FBR) and relatively bulky structures. On reviewing these techniques it became apparent that improved performance could be achieved by combining methods.

To build a wearable electromagnetic belt, a body-matched hybrid loop-dipole antenna was initially designed to achieve directional radiation, wide operating bandwidth, and a compact, light structure. A loop-dipole combination was used to create directional radiation without the need to use an external reflector [27]. The dipole structure is matched to the human body, and thus its structure is miniaturized [28]. The loop structure is miniaturized using Ω-shaped meandered arcs to increase its electrical length without the need for external dielectric loading. Consequently, a wideband antenna operating at 0.58-1.6 GHz with a compact size of $0.096 \times 0.048 \times 0.048\lambda^3$, where λ is the wavelength at the lowest resonance, was achieved.

This antenna is then utilized to build the adjustable wearable electromagnetic belt. The belt is comprised of 12 body matched antennas that are located on a pair of elastic bands that can be adjusted to different body sizes. To verify the performance of the system, a 3D printed phantom was fabricated and filled with tissue-mimicking mixtures to simulate healthy or steatotic liver. The belt system was then used to scan the lower chest, over the region of the liver. The collected signals from the right and left side of the lower chest area were compared using the multivariate energy statistics [29] as a measure of similarity between the left and right sides of this area. The rationale behind this is that any change in the dielectric properties of liver due to hepatic steatosis alters the similarity between left and right sides of this field. The system is experimentally verified to show a notable dissimilarity between healthy and steatotic liver.

The design of a wearable electromagnetic belt involves considering different system blocks such as antenna design, phantom fabrication, data analysis and validation of the system as a unit. Therefore, this paper is organized in different sections. Section II provides a general overview of the concept and building blocks of the system. Section III is devoted to the design and analysis of the proposed antenna. Section IV discusses the design and fabrication of a 3-D phantom, which is used to assess the performance of the antenna and the system. Section V assesses the performance of the proposed antenna and system measurements. Section VI describes the basis of diagnostic method that is utilized to differentiate between different study cases. The simulation and experimental results that prove the potential of the method results are presented in Section VII.

II. THE CONCEPT OF WEARABLE ELECTROMAGNETIC BELT

A schematic of the proposed wearable electromagnetic belt system is depicted in Fig. 1. As seen, this system is comprised of an array of antennas that go around the torso and are connected to each other using a stretchable band. This allows the system to be adjusted to different body shapes. The antennas are connected to a vector network analyzer, which generates the signals to be radiated by the antennas and collects the reflected and transmitted signals. These signals are communicated via a network cable to a computing system, such as a laptop, which also controls the operation of the whole system. The system is designed so that the antennas are symmetrical around the left (L) and right (R) sides of the torso to utilize a comparative detection method. This comparative

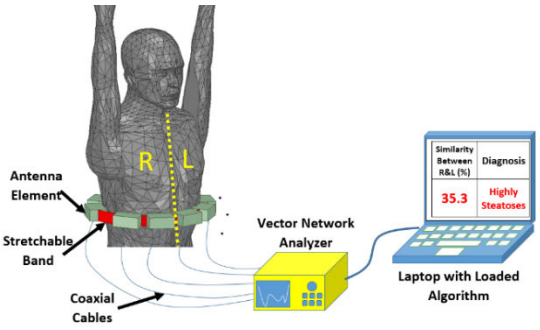

FIGURE 1. A schematic of the proposed wearable electromagnetic belt system.

method is based on the fact that the left and right sides of the torso, around the liver area, have similar dielectric properties. Thus, they are expected to have the highest similarity level in a healthy case in any given test environment. This similarity is expected to be reduced as the liver is infused with fat. This is because the fat has a considerably lower permittivity compared to liver tissue and its surrounding medium. Therefore, by utilizing multivariate energy statistics method, this similarity is calculated and a detection is made based on the obtained similarity value.

It is worth mentioning that at the initial stages of this study, the obtained absolute similarity number is compared to a healthy case, as a reference, to perform detection. However, this requirement will be waived once tests are conducted on higher number of patients and healthy volunteers and a statistically meaningful threshold is created.

III. ANTENNA DESIGN

This section explains different considerations and steps of the antenna design.

A. ANTENNA CONFIGURATION

The first step in the design of the electromagnetic belt, is the design of the scanning antenna. The design criteria for this antenna are:

1) Wide operating bandwidth, which is required in signal processing algorithm to capture changes in the characteristics of the signal over a wide range of frequencies, and thus better resolution.

2) Compact size due to the limited available space for the antenna array and the requirement for reasonable number of antennas to realize acceptable resolution.

3) Unidirectional radiation and peak power delivery deep inside the torso to enable sensing any changes in properties of tissues at that deep area.

To reduce the size and complexity of the electromagnetic belt system and increase the penetration inside lower chest area where liver is located, the dipole antenna is designed to match the anatomy of this region. The dielectric loading from tissues in the lower chest area reduces the size of the antenna, thus allowing locating higher number of them around the region of interest. Consequently, enough information about the internal structure of this area can be obtained. The proposed antenna is depicted in Fig. 2. As seen, the antenna has a three dimensional rectangular-cuboid configuration with the dipole located on the top side of the cube. The main structure of the meandered loop is located at the lower side with its arm expanding on the vertical sides of the cube. All sides of the antenna are printed on 0.8 mm thick FR4 epoxy substrate with permittivity of 4.4 and tangent loss of 0.0026. Generally, body matched antennas are either filled with dielectric material inside their structure, such as dielectric loaded waveguides [30], or immersed in a dielectric matching medium [31]. However, both of those techniques add to the weight of the system, reducing its ease of use in potential clinical setups. To avoid these issues and to miniaturize the antenna, three techniques are adopted in the designed antenna.

To reduce the size of the dipole, it is located in contact with the skin on the chest. The antenna is designed and optimized at the presence of tissues. To represent human body, a large cubic block is used to represent the lower chest, with a side length of 200 mm as shown in Fig. 3. The model has an average permittivity of 45, which is attained by averaging the permittivity of skin, fat, muscle, stomach, spleen according to their thicknesses in an average human body. The size of the block is selected as a compensation between being electrically large, i.e. one wavelength at center frequency, and computational time limitations for simulations. The structure was simulated using Ansys Electronic Desktop (AEDT) 2019.

B. ANTENNA DESIGN GUIDELINES

The design procedure for the proposed hybrid loop-dipole antenna is summarized in 3 steps.

1) The design of body-matched half-wavelength dipole antenna to ensure wide operating bandwidth across the desired frequency band. The antenna is designed and optimized in the presence of torso.
2) Design of the loop structure, which is excited through proximity coupling with the dipole. This approach excites loop-dipole radiation mode and enable the loop to act as a reflector. Hence, it will cancel the back radiation and focus the radiated power towards torso.
3) Meandering loop structure to achieve a compact structure to lower the size and weight of the system and enable positioning larger number of antennas around torso.

Starting from step 1, the initial size of the dipole antenna was calculated using the following formula [28],

$$\lambda = \frac{c}{f \cdot \sqrt{\frac{\varepsilon_{rSubstrate} + \varepsilon_{r,Thorax}}{2}}} \tag{1}$$

and was found to be around 60 mm. The dipole antenna is fed using a coaxial cable. Considering the inevitable effect of the cable on the performance, it is included in the simulation process and is formed as part of the antenna. Therefore, its effect is included on the performance of the antenna. As shown in Fig. 2(a), the center conductor of the coaxial

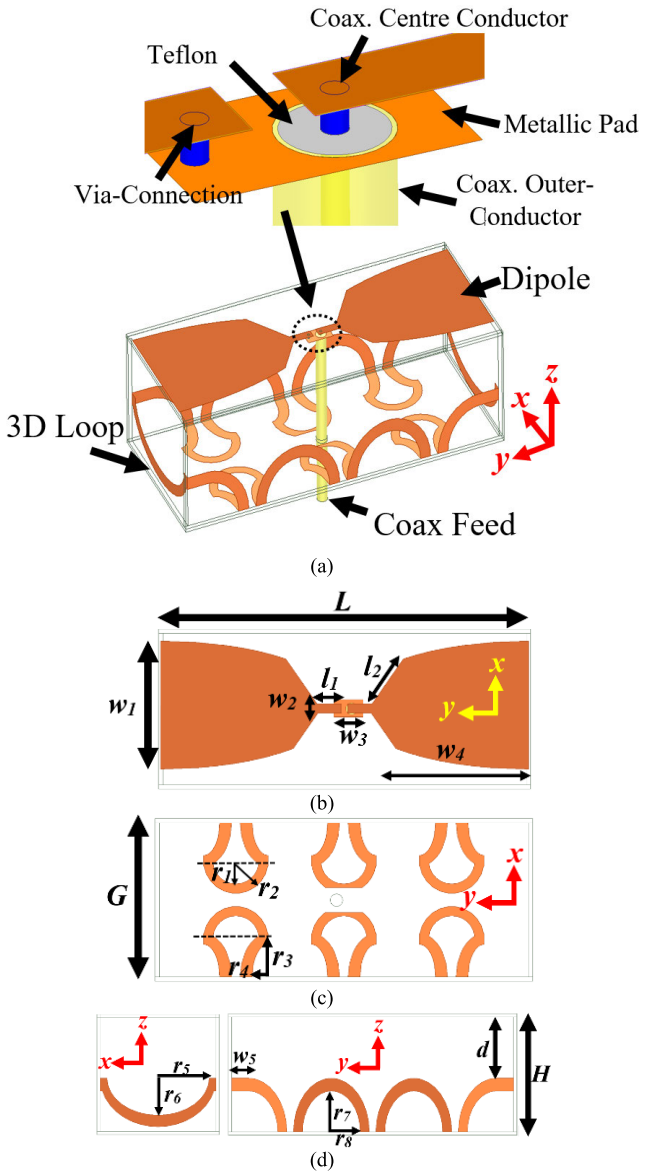

FIGURE 2. (a) 3D configuration of the proposed matched loop-dipole antenna and its (b) Top face, (b) bottom face and (c) side faces. $L = 60$, $G = 30$, $H = 30$, $w_1 = 24$, $w_2 = 1.75$, $w_3 = 5.5$, $w_4 = 24.6$, $w_5 = 4.2$, $l_1 = 4.57$, $l_1 = 10.2$, $r_1 = 3.7$, $r_2 = 5.42$, $r_3 = 7.52$, $r_4 = 3$, $r_5 = 12.5$, $r_6 = 8.96$, $r_7 = 9.8$, $r_8 = 7$, $d = 14.72$. (Unit: mm).

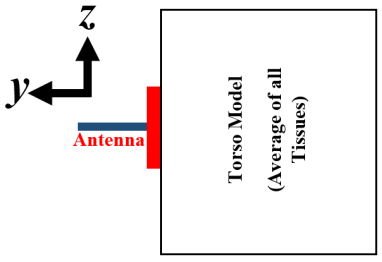

FIGURE 3. Simulation setup configurations.

cable is directly connected to the right side arm of the dipole, whereas the outer conductor (ground) is connected to a small metallic pad with dimensions of 5.5 mm × 3.2 mm at the rear

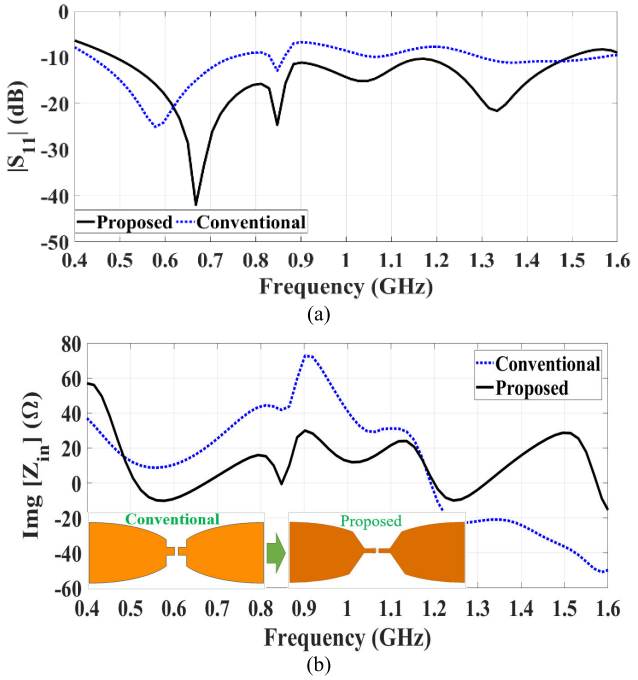

FIGURE 4. (a) $|S_{11}|$ of the designed hybrid loop-dipole antenna and (b) imaginary part of the input impedance.

side of the substrate. The inner and outer conducting layers are separated by a Teflon material. This pad provides ground connection to the left side arm using a via-pin. This feeding structure is designed to enable feeding the dipole from the rear side to provide a seamless contact face for on-body torso scanning. As shown in Fig. 4(a), a semi-elliptical shape was selected for the dipole. This structure has proven to be effective in providing a wide operating frequency band [32]. An area with width of l_1, length of l_2 and angle of 120^0 is carved out of the conventional ellipse (inset of Fig. 4(b)) to compensate for the excessive inductive/capacitive effect of dipole arms on each other at higher frequencies. Consequently, improving the operating bandwidth at 0.87-1.3 GHz (Fig. 4(a)). One of the conventional methods of eliminating antenna's back radiation while enhancing its forward radiation is to locate a reflector at quarter-wavelength distance from the radiating element. While this technique is effective, it dramatically increases the size of the antenna at lower microwave frequencies. Therefore, the second design step is adopted. Accordingly, a loop structure is designed beneath the body matched dipole to excite loop-dipole radiation to direct the irradiated power towards torso. Unlike the dipole structure, the loop is not directly connected to the body. Hence, it cannot be miniaturized using body loading. Considering the large wavelengths at lower microwave frequencies, the conventional folding method would result in large profile for the final design (See Fig. 5(a)). Therefore, to reduce its size, meandering technique is used to increase its electrical size. Thus, the loop structure is wrapped around a rectangular cuboid at a distance d from the dipole and is excited using proximity coupling with the dipole. As seen from Fig. 5(a),

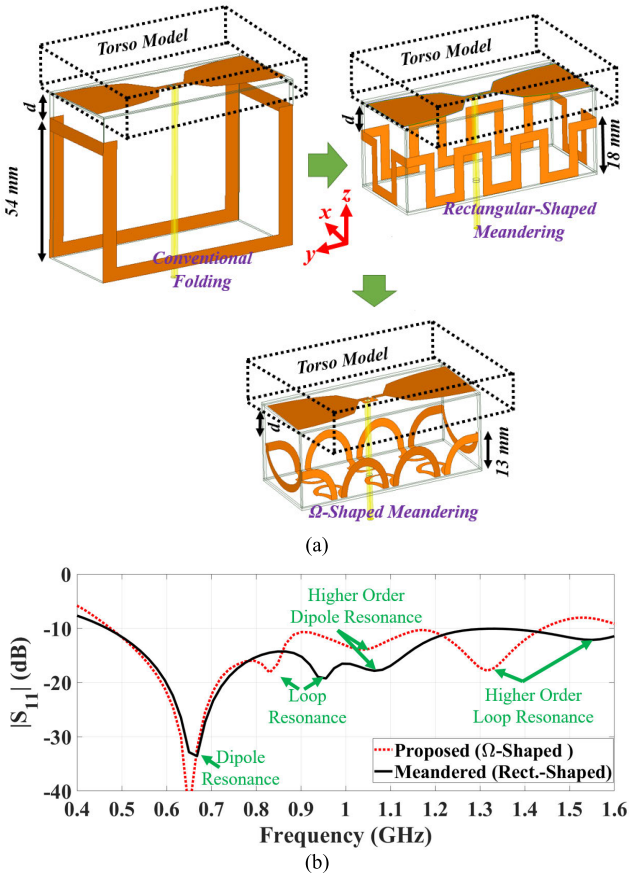

FIGURE 5. (a) Evolution process of the proposed hybrid loop-dipole antenna in the presence of torso. (b) $|S_{11}|$ of the conventional rectangular-shaped meandering vs. the proposed Ω-shaped meandering. d=14.72 mm.

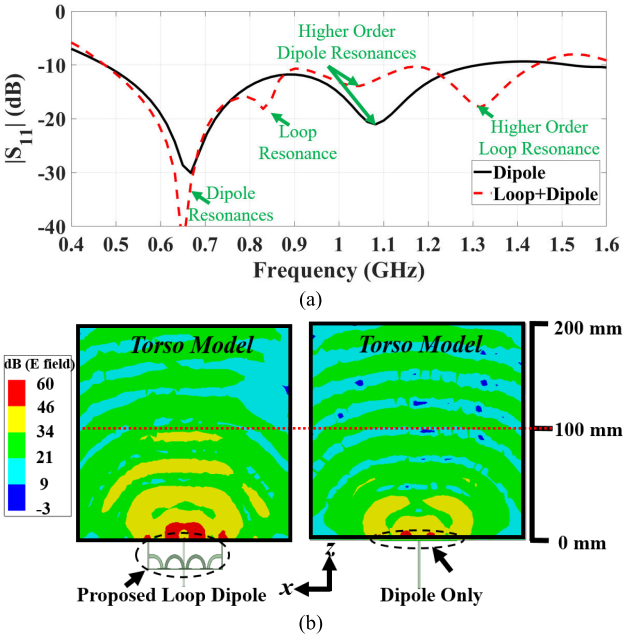

FIGURE 6. (a) $|S_{11}|$ of the body matched dipole vs. proposed hybrid body matched loop-dipole antenna, and (b) their correspondent electric field intensity at sample frequency of 0.84 GHz.

the rectangular shaped meandering reduced the profile of the loop from 54 mm to 18 mm and excites a loop resonance at 0.95 GHz (See Fig. 5(b)). It is known that loop-dipole mode operates at its optimum when loop and dipole modes are close to each other. Hence, a new Ω-shaped meandering is proposed to lower the loop resonance to 0.84 GHz. Unlike conventional rectangular-shaped meandering, Ω-shaped arcs reduce the capacitive coupling between adjacent arms. Therefore, it improves the impedance matching at 1.25-1.4 GHz and reduces the loop profile to 13 mm. The larger side walls are formed using three large ellipses with radii r_7 and r_8, while smaller side walls are formed using single ellipse with radii r_5 and r_6. They are then connected to six Ω-shaped strips that are located on the bottom face of the cuboid. Each Ω-shaped arc is formed by a combination of two half-ellipse and one-half circle shapes (See Fig. 2(c)). As shown in Fig. 6, the design of the loop serves two purposes. Firstly, it widens the impedance matching by excitation of higher order loop mode. The proposed hybrid loop-dipole antenna operates at 0.48-1.6 GHz (Fig. 6(a)). Secondly, it excites the loop resonance at 0.84 GHz, which enhances the intensity of the electric field inside the torso by 13 dB as shown in Fig. 6(b).

The corresponding resonance modes of the proposed antenna are studied in Fig. 7. As seen from inset figures, the dominant surface current occurs on dipole at the lowest resonance, whereas the surface current density is stronger on the loop at the second resonance. By analyzing the current nodes, depicted by O-shape, it is realized that the third resonance is due to second order resonances of the dipole, where strong currents are limited to the area occupied in between nodes, while the outer areas do not contribute to the radiation. Similarly, by analyzing the fourth resonance, it is seen that the four current nodes appear on the loop, representing 2λ mode [33], with weak currents across the majority of each section, contributing weakly to the overall radiation of the antenna.

The size of the human body can vary significantly, resulting in changes in the average medium permittivity seen by the antenna. To verify the robustness of the designed antenna, the permittivity of the torso-emulated medium is altered to 45, 40 and 35. The lower permittivity represents larger body sizes, where the subcutaneous adipose tissue is thicker compared to a lean body. As expected, by reducing the permittivity, the dipole resonance (lower resonance of the antenna) shifts towards higher frequencies, while the loop resonance stays almost constant (See Fig. 8). This is due to the fact that the dipole antenna utilizes the average permittivity of the lower chest area as part of its design to miniaturize its size, whereas the loop's structure is independent of this factor. Nevertheless, all investigated sample cases maintain the wide operating bandwidth of 0.5-1.5 GHz.

C. SIGNAL PENETRATION AND SAR CALCULATIONS

Since the antenna operates in a near to transition field zone and in an on-body configuration, far-field radiation patterns

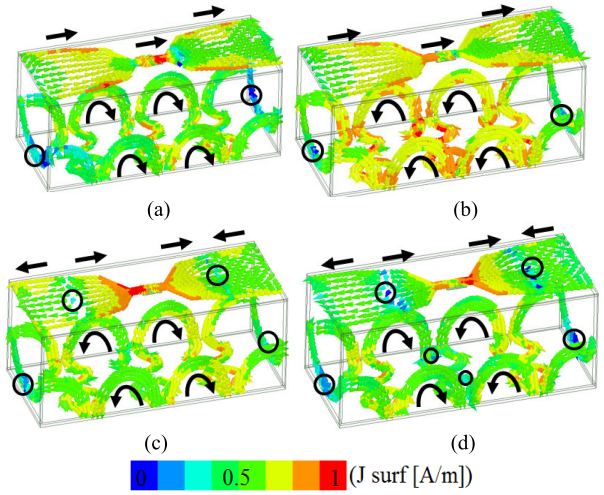

FIGURE 7. Surface current of the proposed antenna at (a) dipole resonance (0.66 GHz), (b) loop-dipole resonance (0.84 GHz), (c) higher order dipole resonance (1.05 GHz) and (d) higher order loop resonance at 1.32 GHz. (O : current node).

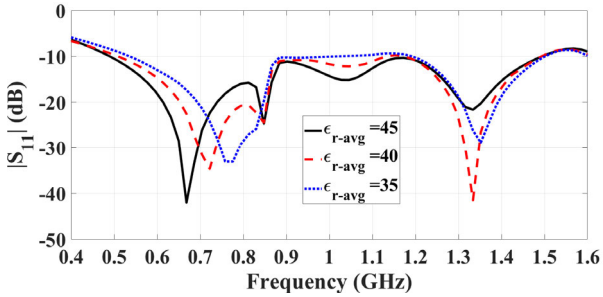

FIGURE 8. Effects of altering the average torso permittivity on the $|S_{11}|$ performance of the antenna.

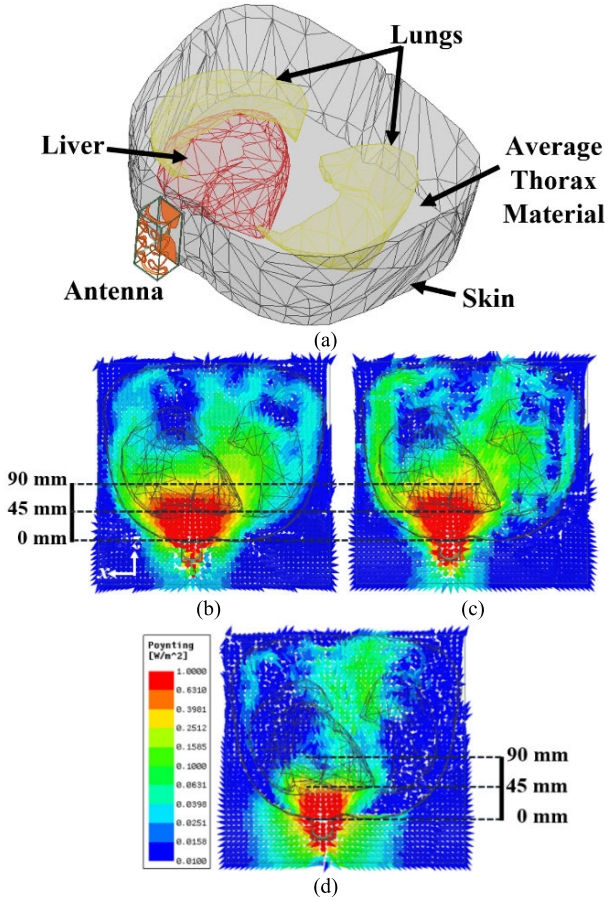

FIGURE 9. (a) Simulation setup. Calculated real part of Poynting vector at sample frequencies of (b) 0.6 GHz, (c) 0.9 GHz and (d) 1.2 GHz.

and gain values are not relevant and meaningful to its operation in this application. Instead, the Poynting vector as a measure of directional energy flux of the electric field is utilized to assess the success of the design in directing maximum energy towards body [5]. As realized from (2), Poynting vector is the time average power density inside the region of interest and has real and imaginary parts, where E and H are the peak instantaneous electric and magnetic field densities, respectively [5].

$$PV_{av} = 1/2[E \times H] \quad (W/m^2) \tag{2}$$

Its real part demonstrates the propagated wave and the imaginary part determines the stored energy. Because the propagated wave is of interest in this application, the real part of this time averaged vector is calculated on a computational phantom in AEDT software. In the simulation setup, depicted in Fig. 9(a), the antenna is located in front of the utilized 3-D phantom including skin, lungs, liver and the average human body tissue that represents fat, muscle and other abdominal tissues. As realized, a vertical slice of the lower chest area, e.g. 100 mm thick, is utilized for computational calculations to reduce the mesh cell size, and hence simulation time and complexity. For the intended torso scanning application, the input power level of 10 dBm, which is considered safe in real-life clinical tests, is utilized. To provide comparable penetration analysis with respect to state of art on-body matched antennas [1], [5], a deep penetration target is set at 70 mm. Fig. 9(b)-(d) represent the calculated values at three sample frequencies 0f 0.6 GHz, 0.9 GHz and 1.2 GHz. The calculated values are normalized to the strongest value to provide an easy comparison at different frequency bands. As seen from Fig. 9(b), the normalized calculated $Re[PV_{av}]$ at 0.6 GHz demonstrates that a peak penetration, e.g. 1 $[W/m^2]$ is achieved at 70 mm inside the lower chest area. Analyzing the density of the signal reveals that the signal can reach center of the liver at a depth of 90 mm, with 64% of the strength of the maximum penetration. This is comparable to exiting designs [1], [5], but with a 60% more compact antenna side length, with respect to the lowest resonance wavelength, enabling positioning of larger number of antennas around body. Fig. 9(b) reveals the same pattern for the strength of the signal at 0.9GHz, where peak loop-dipole mode occurs. As expected, the penetration of the signal weakens significantly at higher frequencies (Fig. 9(c)) due the decrease in the wavelength.

Nevertheless, these signals could be used to analyze abnormalities that are closer to the edge of the region of interest,

e.g. bleedings. The radiation efficiency is one the important parameters in characterizing performance of the antennas. However, because body matched antennas operate in near field zone, conventional radiation efficiency formulas cannot be used/applied. However, Poynting vector analysis can be used to verify that the antenna achieves a unidirectional radiation and the strength of the signal inside the lower chest region of interest is significantly higher compared to the external region. Hence, verifying the efficiency of the antenna in delivering power towards torso.

Lastly, to verify the safety of the utilized antenna on human body, average specific absorption rate (ASAR), which represents the rate that electromagnetic signal is absorbed by human body, is investigated. This study is conducted on the same simulation setup utilized for Poynting vector studies. Peak ASAR value is calculated at 0.6 GHz to be 0.04 [W/kg], well below the safe radiation levels defined by IEEE [34].

IV. PHANTOM FABRICATION

To provide a platform to test the antenna and its capabilities in differentiating healthy and steatotic liver tissue, a 3D water-based phantom is fabricated. This phantom has the realistic size of an average human torso and identical dimensions to the one in simulation setup. The region of interest, encompassing the lower ribs, potentially contains the heart, lungs and diaphragm, along with contents of the upper abdomen including the liver, spleen, stomach, small bowel, pancreas, and kidneys. However, since this prototype is developed aiming to focus on diagnosing hepatic steatosis, the phantom is fabricated to only include liver and its neighboring lungs. The rest of the tissues are represented by an average permittivity medium that fills the area between these organs. Moreover, the outer layer of the phantom is designed in a way that includes skin and fat layers.

A. MODEL DESIGN

To enclose the water-based phantom-mimicking materials a three-dimensional (3D) shell is first designed. To that end, a 3D model is obtained from The Foundation for Research on Information Technologies in Society (IT'IS) Virtual Population (ViP) models. This model includes a detailed whole human body for dosimetric and biomedical applications and is used to obtain the 3D printed model [35]. The CAD file of a male aged 34 years is imported to CST Microwave studio. The STL file is generated and used to develop the 3D printing model of the torso. Due to the size limitation of the selective laser sintering (SLS) 3D printing machine, the STL file was scaled down to 90% of the original Duke model.

The 3D printing of the torso model consists of two parts; the front (i.e., the chest side) and the back sections (See Fig. 10(a)). The back section contains half of the 3D printed structure of liver and lung organs. The other half of these organs are also 3D printed and then glued together to seal the structure. The reason behind this arrangement is to fix the location of lungs and liver and avoid floating structures. To enable filling liver and lung organs with the related tissue

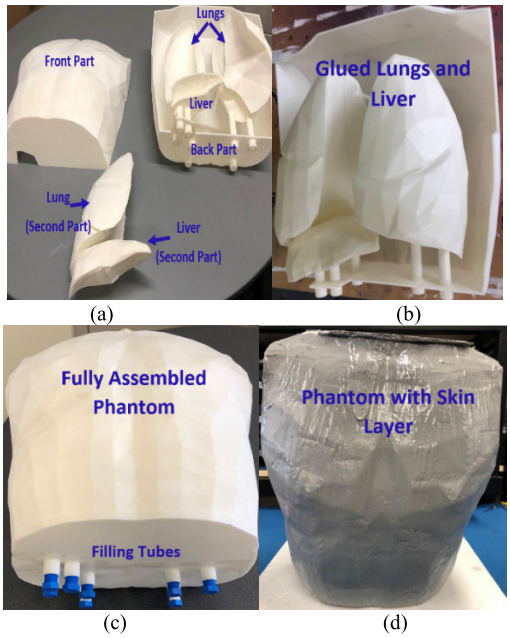

FIGURE 10. (a) The back and the front parts of the torso with the internal structure including the main structure of the liver and lungs and the second parts of lungs and liver. The glued (b) liver and lungs structures and (c) whole phantom structure. (d) Phantom with applied skin layer.

mimicking materials, two tubes are also 3D printed for each lung and liver. One of these tubes is designed to pour the water-based tissue-mimicking material, and the second one is used to provide an air-escape for potential bubbles. Epoxy adhesive is used to seal all the parts and glue them together (Fig. 10(b)). Since the developed phantom utilizes water-based materials, waterproof epoxy is used to avoid any damage resulting from epoxy absorbing water. A water test is performed to make sure there is no leakage from any internal parts (i.e., the liver and lungs models) besides the volume of the average tissue-mimicking materials. The final 3D phantom is shown in Fig. 10(c).

B. DEVELOPMENT OF TISSUES-MIMICKING MATERIALS

To simulate a range of conditions, different solutions are utilized to mimic dielectric properties (permittivity and conductivity) of liver, lungs, and average value for other torso tissues (fat, muscle and bone). The liver solutions include modifications to replicate the degree of hepatic steatosis across the frequency band of 0.5-2 GHz. The fabricated mixtures for healthy tissues utilize the dielectric values obtained from IT'IS website [16]. The 3D-printed outer layer of the phantom is designed to mimic subcutaneous adipose tissue as it has the same dielectric properties as fat. The thickness of this layer is fixed at 3 mm. Polymer composition material composed of epoxy resin reinforced with graphite and aluminum oxide powders are used to fabricate a mimic for skin [36]. The fabricated skin material then used to cover the entire phantom (See Fig. 10(d)).

Water-Based mixtures are then prepared to mimic the rest of the tissues including liver, lungs, average torso, and three

TABLE 1. The dielectric properties of the developed tissue mimicking mixtures and actual tissues Values at 1 Ghz.

Tissue type	Actual Tissues ε_r /σ (S/m)	Mixtures ε_r /σ (S/m)
Skin	40.9/0.89	43.5/1.05
Fat	5.4/0.05	4.2/0.025
Lung (inflated)	21.8/0.47	23/0.95
Liver	46.4/ 0.89	45.5/1.085
Average	N/A	46/1.11

different degrees of hepatic steatosis. Water, glyceride, salt, and/or sugar are used to prepare the mixtures. The mixing ratio of the ingredients depends on the required dielectric properties specification for each tissue. Sodium azide is added to the final recipes as an antibacterial to give the phantom a long life. A Keysight open-ended coaxial dielectric slim probe (N1501A), connected to a Keysight Fieldfox N9926A Vector Network Analyzer (VNA) controlled by a laptop, is utilized to measure the dielectric properties of the mixtures. The three standards of air, short, and water are used to calibrate the probe as reported in [37]. For each tissue-mimicking mixture, multiple measurements are recorded (i.e., six consecutive measurements are taken in different locations) to make sure that the fabricated mixture is homogeneous. Table 1 shows the required and measured dielectric properties of each fabricated tissue type. As seen, the achieved values at the designed frequency of 1 GHz are in reasonable agreement with the actual values. It should be noted that the aim of this study is not to develop a sophisticated phantom but to create a phantom that can reasonably mimic the actual values for relevant tissues. To create the mixtures that mimic the dielectric properties of hepatic steatosis, the values measured using human liver tissues [17] are utilized. Since these values fall within the range 32-40 at 1 GHz, three different mixtures with permittivity of 32, 36 and 40 are prepared. The obtained conductivity values for these cases are 1.1, 1 and 1.15 (S/m), respectively.

V. EXPERIMENTS

This section will present the experimental results.

A. ANTENNA MEASUREMENT

To verify the performance of the proposed body matched antenna, a prototype is fabricated (Fig. 11(a)). It is fed at the centre using a coaxial cable. To maintain the same performance during the measurements ferrite beads were used to suppress surface currents that are induced from the feeding cable from the VNA. This is shown in Fig. 11(a). To avoid damaging the antenna's structure and provide adjustability, a 3D printed case is designed and used. To enclose the antenna (See Fig. 11(a)). The antenna is tested in the presence of neighbouring antennas, and fabricated phantom. To avoid any air gaps between the antenna and the hard-shell phantom, a matching medium was utilized with permittivity of 45, close to that of skin, and conductivity of 0.14 at 1GHz (See Fig. 11(b)). The matching medium is filled inside a thin plastic bag with an open end to allow for expansion of the fluid and release of air bubbles. It should be noted that in practical applications, this matching medium is not required because the antenna can be directly located on skin. The *S*-parameters of the antenna are depicted in Fig. 11(c). As seen, the measured $|S_{11}|$ and $|S_{22}|$ are shifted towards 0.58 MHz in the array configuration with respect to -10 dB reflection coefficient reference value compared to simulations. This is due to the imperfect coupling to the torso phantom and use of low permittivity material to form tissue layers inside the fabricated phantom. Nevertheless, the antenna maintains its wide operating bandwidth across the required operating band.

In EM diagnostic systems, mutual coupling occurs due to three main reasons; 1) Mismatch between the antenna and the imaged object, which causes strong reflections captured by other antennas; 2) The use of common ground, where mutual coupling is cause by propagation of surface waves between the radiators; and 3) the omnidirectional radiation of the antenna, which interferes with the radiation of neighbouring antennas. The proposed structure addresses all these issues by 1) designing of an on-body matched structure that eliminates reflections from skin; 2) utilizing the antennas without common ground; and 3) using the combination of loop-dipole radiation combination to focus the radiated power in one direction. To analyse the mutual coupling between the antennas, $|S_{ij}|$ were measured. As seen from Fig. 11(d), a mutual coupling level less than -18 dB across the bandwidth is achieved. To study the effect of mutual coupling once the belt carrying the antennas is stretched and retracted, the system is simulated using a 25% larger and smaller phantom, respectively, with $|S_{ij}|$ results presented in Fig. 11(e)-(f). It can be realized that the array maintains a mutual coupling blow -20 dB, hence ensuring minimal effect of neighbouring antennas on each other.

B. ELECTROMAGNETIC BELT FABRICATION AND TESTS

After verifying the performance of the proposed antenna design, it is used to build the electromagnetic belt. As shown in the measurement setup in Fig. 12(a), the proof of concept design utilizes elastic bands that simplifies the antenna attachment and location adjustment to the phantom. The elastic band is then pushed through the created holes to build the belt. To cover the circumference of the phantom, 12 antennas are located on the belt and positioned symmetrically with respect to the centre lines of the phantom. The antennas are then connected to 14 port Keysight M9037A PXIe high performance multiport vector network analyser. A schematic of the antennas' locations is depicted in Fig. 12(b). As seen, the plastic bag with matching medium is located between each pair of antennas and skin. To determine the capability of the system to identify hepatic steatosis, four different scenarios are considered, one for healthy liver and three mimicking different degrees of steatosis. The tissue mimicking compartments in the phantom are filled with mixtures that

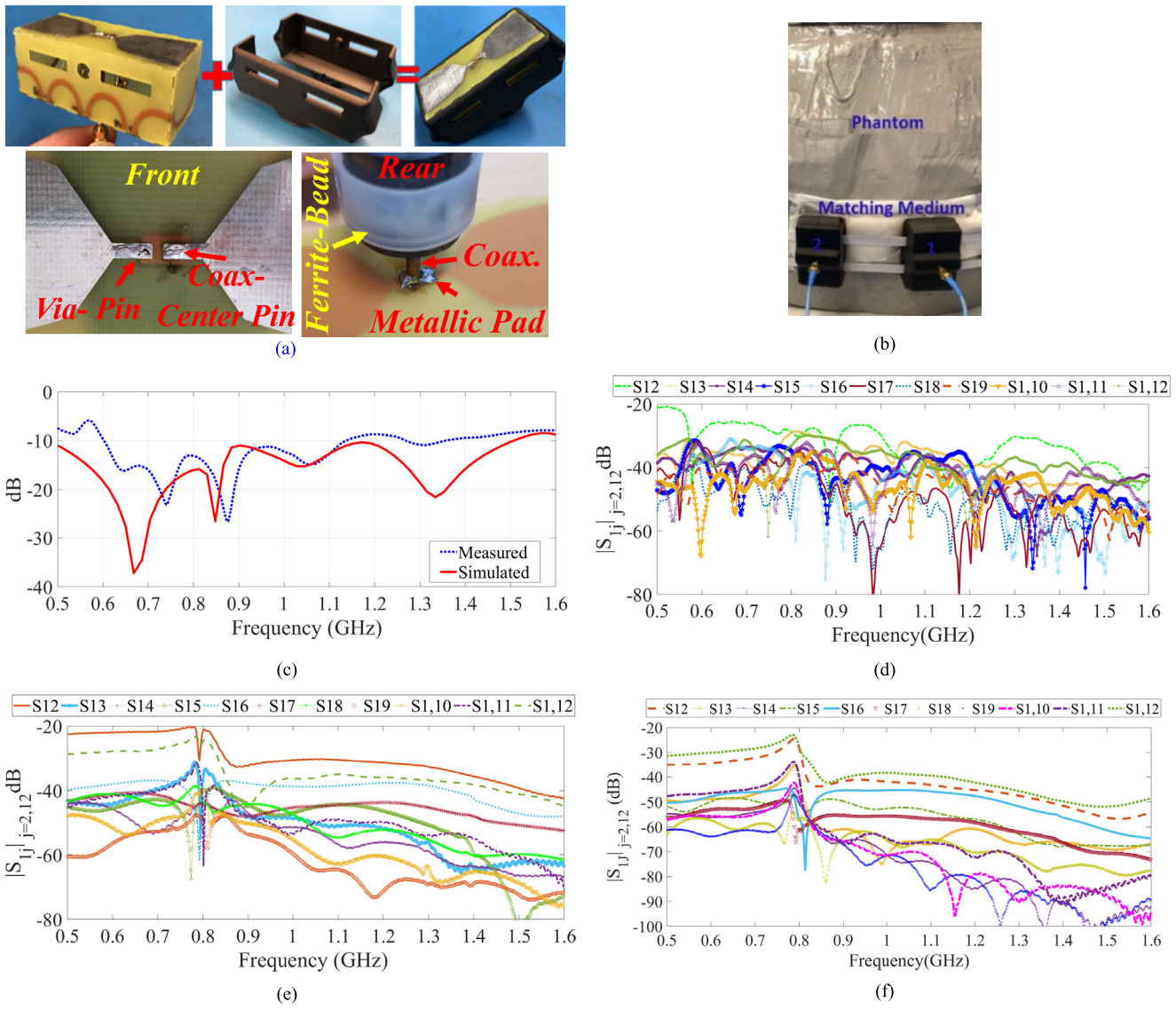

FIGURE 11. (a) Fabricated prototype with its feeding details and its (b) measurement setup. (c) Measured vs. simulated $|S_{11}|$, $|S_{22}|$, $|S_{12}|$ and $|S_{21}|$, (d) measured $|S_{ij}|$ of the fabricated antenna in an array configuration on the phantom; (e) simulated $|S_{ij}|$ on a larger phantom with a 25% size increase; and (f) simulated $|S_{ij}|$ while the antenna is on a smaller phantom with a 25% size reduction.

have dielectric properties as defined in Table 1, including for healthy liver. To create three cases mimicking varying degrees of steatosis, the liquid inside the liver is replaced with mixtures that have average permittivity values of 32, 36 and 40 at 1GHz, respectively. For each case, the system is initiated and a multi-static data acquisition is performed in which each antenna transmits while other antennas are receiving. This procedure is repeated for all 12 antennas till a full scan is performed. Each measurement is repeated four times with a duration of less than 10 seconds.

VI. STATISTICAL METHOD FOR DISTINGUISHING BETWEEN HEALTHY LIVER AND HEPATIC STEATOSIS

Based on previous measurements, as the degree of hepatic steatosis increases, the hepatic permittivity decreases [17]. Thus, a comparative analysis method is utilized in this paper to distinguish between healthy and steatotic liver. This method utilizes the differences in reflected/transmitted signals between the right side of the body, where the liver is located, and the left side of the body, where lungs and average tissue properties are present. Considering the similarity of permittivity values for healthy liver and its neighbouring tissues, signals from the right and left side of the body are similar. Hepatic steatosis alters the dielectric properties of the liver and the similarity in results between both sides of the body are lost. This could be used to detect and quantify the degree of steatosis.

To investigate this concept, we here propose multivariate distance correlation statistics [29] as a metric for measuring the similarity between the left and right sides of body

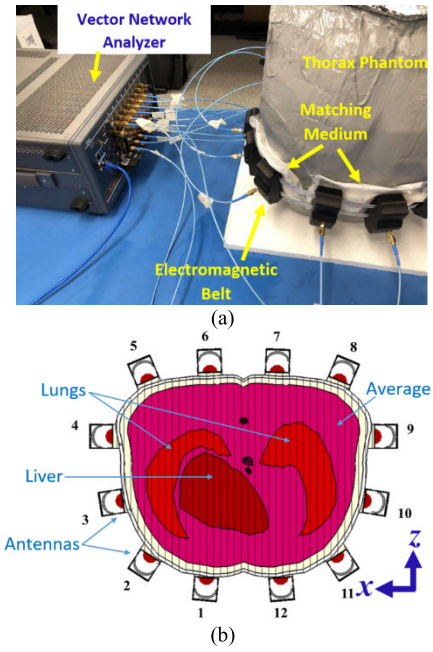

FIGURE 12. (a) Measurement Setup and (b) schematic configuration.

for different dielectric properties of liver tissue. This metric can be applied as similarity measure between a sample and a hypothesized distribution, or the difference between two or more arbitrarily selected samples that do not necessarily have equal dimensions.

Distance correlation (*dCorr*) of two random vectors **x** and **y** is defined by:

$$R_N^*(\boldsymbol{x},\boldsymbol{y}) = \frac{\nu_N^*(\boldsymbol{x},\boldsymbol{y})}{\sqrt{\nu_N^*(\boldsymbol{x})\nu_N^*(\boldsymbol{y})}},$$
$$\nu_N^*(\boldsymbol{x},\boldsymbol{y}) = \frac{\mathbf{1}}{N^2}\sum\nolimits_{k,l=1}^{N} A_{kl}B_{kl} \tag{3}$$

where $\nu_N^*(\boldsymbol{x},\boldsymbol{y})$ is empirical covariance and $A_{kl}B_{kl}$ coefficients computed as $A_{kl} = a_{kl} - \overline{a_{k.}} - \overline{a_{.l}} + \overline{a_{..}}$, $B_{kl} = b_{kl} - \overline{b_{k.}} - \overline{b_{.l}} + \overline{b_{..}}$, $a_{kl} = \left\|\boldsymbol{x}^k - \boldsymbol{x}^l\right\|$, $b_{kl} = \left\|\boldsymbol{y}^k - \boldsymbol{y}^l\right\|$, $\overline{a_{k.}} = \frac{1}{N}\sum_{l=1}^{N} a_{kl}$, $\overline{a_{.l}} = \frac{1}{N}\sum_{k=1}^{N} a_{kl}$, $\overline{a_{..}} = \frac{1}{N^2}\sum_{k,l=1}^{N} a_{kl}$, $\overline{b_{k.}} = \frac{1}{N}\sum_{l=1}^{N} b_{kl}$, $\overline{b_{.l}} = \frac{1}{N}\sum_{k=1}^{N} b_{kl}$ and $\overline{b_{..}} = \frac{1}{N^2}\sum_{k,l=1}^{N} b_{kl}$,

It satisfies below defined conditions:

1) $0 \le R_N^*(\boldsymbol{x},\boldsymbol{y}) \le 1$
2) *If* $R_N^*(\boldsymbol{x},\boldsymbol{y}) = 1$,

then there exists a vector b, a non-zero real number k and an orthogonal matrix C such that $\boldsymbol{y} = k\boldsymbol{x}C + b$, for the data matrices of $\boldsymbol{x}$ and $\boldsymbol{y}$. Besides being suitable for vectors of arbitrary sizes and distributions, this method is also capable to capture nonlinear relationships [38]. This characteristic provides an advantage over other statistical metrics that are used for measuring similarity in data.

Original data in frequency domain is transformed to time domain by applying inverse Fourier transformation and the obtained time series are mapped to a network. The advantages of applying this process are; firstly, the structural patterns at different time scales from microscopic to macroscopic levels can be visually investigated [39]. Secondly, it is suitable for analysis of non-stationary time series similar to the proposed application. *Visibility graph* (*VG*) method [39] is utilized to map time domain signals to a graph. It generates a graph based on visibility criteria given by:

$$y_A < y_B + (y_A - y_B)\frac{t_B - t_C}{t_B - t_A} \tag{4}$$

where indices A, B and C denote data points of time series characterized by its value y at time instance. It follows that two arbitrary data points (t_A, y_A) and (t_B, y_B) will have visibility, and thus will become two connected nodes of the associated graph, if any other data point (t_C, y_C) placed between them fulfills inequality (4).

VII. RESULTS

This section describes the results of applying the proposed analytical method on data that are obtained using *CST* simulations and phantom measurements.

The proposed method have been tested on matrices comprising four signals, i.e. $S_{4xN_F}^R = \left[\boldsymbol{S_{5,1}S_{6,1}S_{5,2}S_{6,2}}\right]$, $S_{4xN_F}^L = \left[\boldsymbol{S_{8,12}S_{7,12}S_{8,11}S_{7,11}}\right]$. The four signals (*S*-parameters) composing the $S_{4xN_F}^R$ are chosen based on the location of their corresponding transmitter and receiver antennas i.e. in front and back of the liver. The signals of $S_{4xN_F}^L$ are the symmetric counterparts of $S_{4xN_F}^R$. As analyzed in Section II, the penetration of the antenna at frequencies above 1 GHz is not suitable for deep targets. These frequencies are utilized for imaging applications where higher frequencies enhance the contrast of the formed images. Nevertheless, the frequency range 0.5-1 GHz is considered and the *VG*s are computed using 500 points of the obtained time domain signals. Obtained results are computed for three permittivity values mimicking differing degrees of hepatic steatosis and one for normal liver tissue in the form of percentage obtained by scaling the computed statistics by 100%. The rationale for interpreting results is that the highest value of the computed statistics indicates highest similarity between the left and right side of the body slice. This occurs when the liver is not steatotic. Consequently, in presence of hepatic steatosis, this similarity will be distorted/reduced.

A. CST SIMULATION RESULTS

To emulate hepatic steatosis in the simulation environment, the dielectric properties of healthy liver is altered in the CST simulation model shown in Fig. 12(b). Results reported in Table 2 indicate that there is a meaningful difference between the signals collected for healthy and steatotic liver. As seen, when the permittivity value is 45, the similarity between left and right sides of the lower chest area achieve the highest values of 77.2%. This similarity decreases as the permittivity value is reduced to 40, 36 and 32 for emulated hepatic steatosis. For instance, the similarity for the case with permittivity of 40 is 68.9%. This represents normalized difference of 10.7% with respect to the healthy case. Yet, this

TABLE 2. Similarity percent of left and right side of the torso on the simulation and experimental data.

ε_{liver}	*Similarity* [%]	
	Simulation	*Measurement 1*
45	77.2	41.6
40	68.9	39.2
36	40.63	35.4
32	35.5	35.3

dissimilarity in the case with permittivity of 32 drastically increases to 54% with respect to healthy case.

B. PHANTOM MEASUREMENT RESULTS

To validate simulation results, the proposed approaches are tested for the detection of hepatic steatosis on experimental data obtained as discussed in Section IV.B and presented in Table 2. Though being quantitatively different from the simulation results, the proposed method attains minimum dissimilarity of 5.5% (in the case with permittivity of 40) with respect to the healthy case. This dissimilarity increases to 15.1% for a severe NAFLD case. As realized, the obtained results from measurements provide closer values compared to simulations. The main reason for dissimilarities is the non-identical measurement and simulation setup. In the simulations, the used model includes all the torso tissues with their realistic anatomy and dielectric properties. In the measurements, we built and used a phantom that includes only the main tissues due to complexity of human torso, which includes many overlapped tissues. Moreover, the inner organs of the phantom, such as lungs and liver, were built using low-dielectric constant shells to hold and separate liquid from torso tissue. The utilized mixtures in the phantom have reasonably close dielectric properties to the simulated model, but with some differences across the wide utilized band. Hence, while we acknowledge this discrepancy, the main objective of this study is to show the feasibility of applying this method and not comparing simulated vs. measured results due to the differences in the tested environment. Nevertheless, the obtained results considering 6 case studies (simulation and measurement combination) reveal that the comparison of the symmetrical signals of the left and right sides of over the liver can be exploited for potentially distinguish between healthy and steatotic liver.

C. REPEATABILITY, STABILITY AND RELIABILITY ANALYSIS

To verify the repeatability of using the system, the measurement was repeated four times for each case and the peak variance between obtained signals, e.g. *S*-parameters, is calculated and found to be 1 dB (See Fig. 13(a)). To calculate the stability of the system and its resilience towards potential misalignments of antennas, the antennas are randomly misaligned by 1-3 mm from their original symmetric position. The obtained variance in measurements between the symmetric and non-symmetric system is calculated and found to be less than 6 dB across the majority of the band.

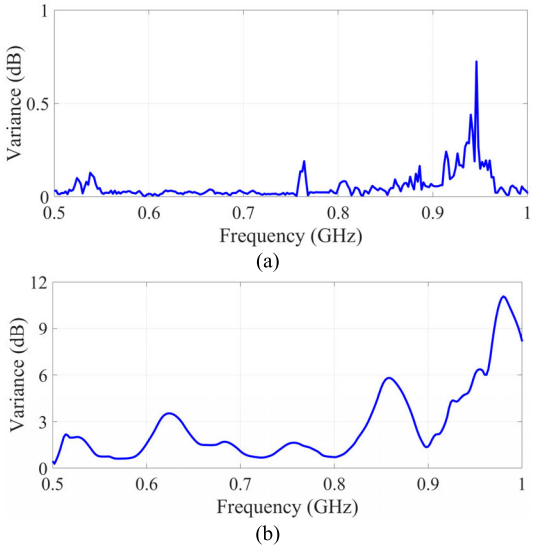

FIGURE 13. Variance of data in (a) repeated measurements in a symmetric left/ right structure and (b) measurements between symmetric and asymmetric system.

TABLE 3. Similarity between left and right side of the torso on asymmetric experimental data.

ε_{liver}	*Similarity* [%]
45	45.16
40	38.02
36	37.17
32	36.42

TABLE 4. Similarity between left and right side of the torso on two simulated phantoms with different sizes.

ε_{liver}	*Similarity* [%]	
	Small Phantom	*Large Phantom*
45	55.3	57.5
32	47.6	34.1

The similarities of results between left and right side of the torso for the non-symmetric system are presented in Table 3. As seen, the algorithm can successfully distinguish between healthy and disease cases, yet these values are different from the first experiment in Table 2. It should be noted that in this system, the stability of the system is defined as its ability to distinguish between healthy and steatotic liver rather than obtaining exact the same value each time.

To investigate the reliability of the proposed algorithm to differentiate between healthy and steatotic liver, two scenarios were considered. In the first, the size of the phantom was decreased by 25% and simulations were conducted for a healthy liver and severe steatotic liver with permittivity of 32. The same process was repeated for the second scenario but with a 25% increased phantom size. The obtained results are presented in Table 4. As shown, the algorithm can successfully distinguish between healthy and steatotic liver in both scenarios. While this system is adjustable, it is limited to

60% size increase from the average in which the peak power (See-Fig. 9) can reach the liver structure.

VIII. CONCLUSION

An electromagnetic belt for the detection steatotic liver, a cardinal feature of NAFLD, has been presented. The belt is comprised of twelve three-dimensional hybrid antennas. Each antenna utilizes body matched dipole and three-dimensional meandered loop structure to achieve compact size, unidirectional radiation and wideband. The proposed antenna operates across the band 0.58-1.6 GHz, which is adopted for biomedical electromagnetic imaging. To verify the capability of the imaging belt, a 3D printed phantom is fabricated and filled with tissue mimicking mixtures and different healthy and disease scenarios. Considering the close proximity of the dielectric properties of liver to its surrounding tissues, lower chest symmetry is exploited as a base for detecting hepatic steatosis. This is achieved by measuring the similarity between the symmetrical signals on the left and the right side of the scanned slice and comparing them to results from normal liver. Multivariate distance correlation statistics method is used to analyze the collected signals. The obtained results demonstrate significant dissimilarity between steatotic and non-steatotic liver, indicating the significant potential of the proposed belt.

REFERENCES

[1] A. S. M. Alqadami, K. S. Bialkowski, A. T. Mobashsher, and A. M. Abbosh, "Wearable electromagnetic head imaging system using flexible wideband antenna array based on polymer technology for brain stroke diagnosis," *IEEE Trans. Biomed. Circuits Syst.*, vol. 13, no. 1, pp. 124–134, Feb. 2019, doi: 10.1109/TBCAS.2018.2878057.

[2] H. Zhang, "Microwave imaging for breast cancer detection: The discrimination of breast lesion morphology," *IEEE Access*, vol. 8, pp. 107103–107111, 2020.

[3] J.-K. Wang, X. Jiang, L. Peng, X.-M. Li, H.-J. An, and B.-J. Wen, "Detection of neural activity of brain functional site based on microwave scattering principle," *IEEE Access*, vol. 7, pp. 13468–13475, 2019.

[4] D. Yang, Z. Zhu, and B. Liang, "Vital sign signal extraction method based on permutation entropy and EEMD algorithm for ultra-wideband radar," *IEEE Access*, vol. 7, pp. 178879–178890, 2019.

[5] H. Bahramiabarghouei, E. Porter, A. Santorelli, B. Gosselin, M. Popovic, and L. A. Rusch, "Flexible 16 antenna array for microwave breast cancer detection," *IEEE Trans. Biomed. Eng.*, vol. 62, no. 10, pp. 2516–2525, Oct. 2015.

[6] M. Persson, A. Fhager, H. D. Trefna, Y. Yu, T. McKelvey, G. Pegenius, J.-E. Karlsson, and M. Elam, "Microwave-based stroke diagnosis making global prehospital thrombolytic treatment possible," *IEEE Trans. Biomed. Eng.*, vol. 61, no. 11, pp. 2806–2817, Nov. 2014.

[7] K. Kanazawa, K. Noritake, Y. Takaishi, and S. Kidera, "Microwave imaging algorithm based on waveform reconstruction for microwave ablation treatment," *IEEE Trans. Antennas Propag.*, vol. 68, no. 7, pp. 5613–5625, Jul. 2020, doi: 10.1109/TAP.2020.2972633.

[8] P. T. Nguyen, A. M. Abbosh, and S. Crozier, "3-D focused microwave hyperthermia for breast cancer treatment with experimental validation," *IEEE Trans. Antennas Propag.*, vol. 65, no. 7, pp. 3489–3500, Jul. 2017.

[9] A. Zamani, S. A. Rezaeieh, and A. M. Abbosh, "Lung cancer detection using frequency-domain microwave imaging," *Electron. Lett.*, vol. 51, no. 10, pp. 740–741, May 2015.

[10] S. Ahdi Rezaeieh, A. Zamani, K. S. Bialkowski, and A. M. Abbosh, "Novel microwave torso scanner for thoracic fluid accumulation diagnosis and monitoring," *Sci. Rep.*, vol. 7, no. 1, p. 304, Dec. 2017.

[11] C. Susskind, "Possible use of microwaves in the management of lung disease," *Proc. IEEE*, vol. 61, no. 5, pp. 673–674, May 1973.

[12] A. Zamani, A. M. Abbosh, and A. Toaha Mobashsher, "Fast frequency-based multistatic microwave imaging algorithm with application to brain injury detection," *IEEE Trans. Microw. Theory Techn.*, vol. 64, no. 2, pp. 653–662, Feb. 2016.

[13] A. Brankovic, A. Zamani, and A. Abbosh, "Electromagnetic based fatty liver detection using machine learning," in *Proc. 13th Eur. Conf. Antennas Propag. (EuCAP)*, Krakow, Poland, 2019, pp. 1–3.

[14] *Nonalcoholic Fatty Liver Disease—A Growing Public Health Problem, World Gastroenterology Organization*. Accessed: Aug. 3, 2020. [Online]. Available: https://www.worldgastroenterology.org/publications/e-wgn/e-wgn-expert-point-of-view-articles-collection/nonalcoholic-fatty-liver-disease-a-growing-public-health-problem

[15] *EASL-EASD-EASO Clinical Practice Guidelines for the Management of Non-Alcoholic Fatty Liver Disease*. Accessed: Aug. 3, 2020. [Online]. Available: https://www.journal-of-hepatology.eu/article/S0168-8278(15)00734-5/abstract

[16] *Tissue Properties Database, The Foundation for Research on Information Technologies in Society (IT'IS)*. Accessed: Aug. 3, 2020. [Online]. Available: https://itis.swiss/virtual-population/tissue-properties/database/tissue-frequency-chart/

[17] A. Peyman, B. Kos, M. Djokić, B. Trotovšek, C. Limbaeck-Stokin, G. Serša, and D. Miklavčič, "Variation in dielectric properties due to pathological changes in human liver," *Bioelectromagnetics*, vol. 36, no. 8, pp. 603–612, Oct. 2015.

[18] S. Ahdi Rezaeieh, Y.-Q. Tan, A. Abbosh, and M. A. Antoniades, "Equivalent circuit model for finding the optimum frequency range for the detection of heart failure using microwave systems," in *Proc. IEEE Antennas Propag. Soc. Int. Symp. (APSURSI)*, Orlando, FL, USA, Jul. 2013, pp. 2059–2060.

[19] N. Celik, R. Gagarin, H.-s. Youn, and M. F. Iskander, "A noninvasive microwave sensor and signal processing technique for continuous monitoring of vital signs," *IEEE Antennas Wireless Propag. Lett.*, vol. 10, pp. 286–289, 2011.

[20] M. Zada, I. A. Shah, and H. Yoo, "Metamaterial-loaded compact high-gain dual-band circularly polarized implantable antenna system for multiple biomedical applications," *IEEE Trans. Antennas Propag.*, vol. 68, no. 2, pp. 1140–1144, Feb. 2020, doi: 10.1109/TAP.2019.2938573.

[21] S. Ahdi Rezaeieh, M. A. Antoniades, and A. M. Abbosh, "Miniaturization of planar yagi antennas using mu-negative metamaterial-loaded reflector," *IEEE Trans. Antennas Propag.*, vol. 65, no. 12, pp. 6827–6837, Dec. 2017.

[22] X. Zhu, J. Zhang, T. Cui, and Z. Zheng, "A dielectric-loaded dual-broadband printed dipole antenna with stable radiation pattern in the H-Plane," *IEEE Antennas Wireless Propag. Lett.*, vol. 18, no. 9, pp. 1761–1765, Sep. 2019.

[23] M. Yang, Y. Pan, and W. Yang, "A singly fed wideband circularly polarized dielectric resonator antenna," *IEEE Antennas Wireless Propag. Lett.*, vol. 17, no. 8, pp. 1515–1518, Aug. 2018.

[24] S. Ahdi Rezaeieh, A. Abbosh, and Y. Wang, "Wideband unidirectional antenna of folded structure in microwave system for early detection of congestive heart failure," *IEEE Trans. Antennas Propag.*, vol. 62, no. 10, pp. 5375–5381, Oct. 2014.

[25] W. Zhang, Y. Li, Z. Zhou, and Z. Zhang, "Dual-mode compression of dipole antenna by loading electrically small loop resonator," *IEEE Trans. Antennas Propag.*, vol. 68, no. 4, pp. 3243–3247, Apr. 2020, doi: 10.1109/TAP.2019.2948712.

[26] S. Ahdi Rezaeieh, K. S. Bialkowski, A. Zamani, and A. M. Abbosh, "Loop-dipole composite antenna for wideband microwave-based medical diagnostic systems with verification on pulmonary edema detection," *IEEE Antennas Wireless Propag. Lett.*, vol. 15, pp. 838–841, 2016.

[27] W.-J. Lu, W.-H. Zhang, K. F. Tong, and H.-B. Zhu, "Planar wideband loop-dipole composite antenna," *IEEE Trans. Antennas Propag.*, vol. 62, no. 4, pp. 2275–2279, Apr. 2014.

[28] X. Li, M. Jalilvand, Y. L. Sit, and T. Zwick, "A compact double-layer on-body matched bowtie antenna for medical diagnosis," *IEEE Trans. Antennas Propag.*, vol. 62, no. 4, pp. 1808–1816, Apr. 2014.

[29] G. J. Székely and M. L. Rizzo, "Brownian distance covariance," *Ann. Appl. Statist.*, vol. 3, no. 4, pp. 1236–1265, 2009.

[30] M. Hamid, "Dielectric loaded horn antennas having improved radiation characteristics," U.S. Patent 4 447 811, May 8, 1984.

[31] V. Zhurbenko, T. Rubæk, V. Krozer, and P. Meincke, "Design and realisation of a microwave three-dimensional imaging system with application to breast-cancer detection," *IET Microw., Antennas Propag.*, vol. 4, no. 12, pp. 2200–2211, Dec. 2010.

[32] Z. Tu, D.-F. Zhou, G.-Q. Zhang, F. Xing, X. Lei, and D.-W. Zhang, "A wideband cavity-backed elliptical printed dipole antenna with enhanced radiation patterns," *IEEE Antennas Wireless Propag. Lett.*, vol. 12, pp. 1610–1613, 2013.
[33] H. Xu, H. Wang, S. Gao, H. Zhou, Y. Huang, Q. Xu, and Y. Cheng, "A compact and low-profile loop antenna with six resonant modes for LTE smartphone," *IEEE Trans. Antennas Propag.*, vol. 64, no. 9, pp. 3743–3751, Sep. 2016.
[34] (1998). *IEEE Committee on Radiation Technical Information Statement on Human Exposure to Microwaves and Other Radio Frequency EM Fields*. Accessed: Aug. 3, 2020. [Online]. Available: http://ewh.ieee.org/soc/embs/comar/rf_mw.htm/
[35] P. Hasgall, F. Di Gennaro, C. Baumgartner, E. Neufeld, M. Gosselin, D. Payne, A. Klingenbock, and N. Kuster. (May 2018). *IT'IS Database for Thermal and Electromagnetic Parameters of Biological Tissues, Version 4.0*. [Online]. Available: https://itis.swiss/virtual-population/tissue-properties/overview/, doi: 10.13099/VIP21000-04-0.
[36] J. Garrett and E. Fear, "A new breast phantom with a durable skin layer for microwave breast imaging," *IEEE Trans. Antennas Propag.*, vol. 63, no. 4, pp. 1693–1700, Apr. 2015.
[37] S. Gabriel, R. W. Lau, and C. Gabriel, "The dielectric properties of biological tissues: II. Measurements in the frequency range 10 Hz to 20 GHz," *Phys. Med. Biol.*, vol. 41, no. 11, p. 2251, 1996.
[38] A. Brankovic, M. Hosseini, and L. Piroddi, "A distributed feature selection algorithm based on distance correlation with an application to microarrays," *IEEE/ACM Trans. Comput. Biol. Bioinf.*, vol. 16, no. 6, pp. 1802–1815, May 2018.
[39] Donner RV, Heitzig J, Donges JF, Zou Y, Marwan N, Kurths J, "The geometry of chaotic dynamics—A complex network perspective," *Eur. Phys. J. B*, vol. 84, pp. 653–672, Dec. 2011.
[40] L. Lacasa, B. Luque, F. Ballesteros, J. Luque, and J. C. Nuno, "From time series to complex networks: The visibility graph," *Proc. Nat. Acad. Sci. USA*, vol. 105, no. 13, pp. 4972–4975, 2008.

SASAN AHDI REZAEIEH (Member, IEEE) received the Ph.D. degree from The University of Queensland, Australia, in 2016, where he worked on design of various clinical prototypes for fluid accumulation detection inside human torso. His research interests include design and miniaturization of several types of metamaterial antennas, wideband and unidirectional antennas, three dimensional structures, and biomedical platform and system designs. He was a recipient of the IEEE Antennas and Propagation Society Doctoral Research Award, in 2014, and the IEEE Antennas and Propagation Letters Outstanding Reviewer Award, in 2018.

AIDA BRANKOVIC (Member, IEEE) received the bachelor's and master's degrees in automation, control and electronics from the University of Sarajevo, Sarajevo, Bosnia and Herzegovina, in 2009 and 2011, respectively, and the Ph.D. degree from the Systems and Control Division, Dipartimento di Elettronica, Informazione e Bioingegneria, Politecnico di Milano, Milan, Italy, in 2018. In academic 2012–2013, she was a Teaching Assistant with the Electrical Faculty, University of Sarajevo. In the end of 2013, she joined the MOVE Research Group, Politecnico di Milano, for two years, and afterwards continues her Ph.D. at the Dipartimento di Elettronica, Informazione e Bioingegneria. In 2018, she joined the Electromagnetic Research Group, The University of Queensland. Her current interests include nonlinear model identification, randomized algorithms, and statistical machine learning.

AZIN S. JANANI received the B.S. and M.S. degrees in biomedical engineering from Amirkabir University (Tehran Poly-Technique), Iran, in 2008 and 2010 respectively, and the Ph.D. degree from Flinders University, Australia, in 2019. In 2019, she joined the Electromagnetic Research Group, The University of Queensland. Her research interests include biomedical signal processing, disease classification, and computer aided diagnosis system development. She was a recipient of the Australian Endeavour Postgraduate Scholarship, in 2016, for her Ph.D. studies.

BEADAA MOHAMMED (Member, IEEE) received the B.Sc. and M.Sc. degrees in electrical engineering and electronics and communication engineering from Mosul University, Mosul, Iraq, in 1994 and 2002, respectively, and the Ph.D. degree in electrical engineering from the School of Information Technology and Electrical Engineering, The University of Queensland, Australia, in 2015. She is currently a Postdoctoral Fellow with the School of Information Technology and Electrical Engineering, The University of Queensland. Her current research interest includes developing components for electromagnetic imaging systems for medical applications.

AMIN DARVAZEHBAN (Student Member, IEEE) received the B.Sc. degree in electrical engineering from Shahid Beheshti University, Tehran, Iran, in 2011, and the M.S. degree from the Amirkabir University of Technology, Tehran, in 2013. He is currently pursuing the Ph.D. degree with the Electromagnetic Innovations (εMAGin) Group, School of Information Technology and Electrical Engineering, The University of Queensland, Australia. He was a Researcher with the Electromagnetic and Nondestructive Testing Laboratory, Amirkabir University of Technology, from 2013 till 2017. His current research interests include the design of biomedical antennas, beam forming networks, metasurfaces, and pattern reconfigurable antennas.

ALI ZAMANI (Member, IEEE) received the B.S. degree in electronics engineering from Isfahan University, Iran, in 2008, the M.S. degree in electrical engineering from the Iran University of Science Technology, in 2012, and the Ph.D. degree from The University of Queensland, Australia, in 2018. In 2014, he joined the Electromagnetic Research Group, The University of Queensland. His research interests include computational electromagnetics, signal processing, and microwave imaging. He was a recipient of the Australian Endeavour Postgraduate Scholarship in 2014 for his PhD studies. He was also awarded the Candidate Development Award in 2017, the Richard Jago Memorial Prize in 2016, and the Maude Walker Scholarship in 2014 from The University of Queensland for his research achievements in the field of electromagnetic imaging.

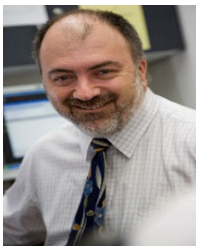

GRAEME A. MACDONALD is currently a Senior Staff Specialist with the Department of Hepatology and Gastroenterology, Princess Alexandra Hospital, and a member of the Queensland Liver Transplant Service. His clinical interests are predominantly in liver disease and he provides clinical services in general hepatology, and the care of patients' pre- and post-liver transplantation. His research interests include obesity-related liver injury and liver transplantation. He received peer-reviewed funding form the National Health and Medical Research Council, the Cancer Council of Queensland, and other funding bodies. He has published over 80 articles and book chapters in the area of liver disease.

AMIN M. ABBOSH (Senior Member, IEEE) leads the Electromagnetic Group. He is currently the Head of the School of ITEE, The University of Queensland, Brisbane, QLD, Australia. He has authored more than 400 articles on electromagnetic imaging systems for medical applications, wideband passive microwave devices, and planar antennas. His coauthored article in Optimization-Based Confocal Microwave Imaging in Medical Applications, the IEEE TRANSACTIONS ON ANTENNAS AND PROPAGATION, and received IEEE APS King Award for best paper published in 2015 and 2020. As recognition of his international research standing, he was awarded with the Higher Doctorate (Doctor of Engineering) by The University of Queensland, in 2013. He is also an Associate Editor of the IEEE TRANSACTIONS ON ANTENNAS AND PROPAGATION and IEEE ANTENNAS AND WIRELESS PROPAGATION LETTERS.